Inhibition of EBV-mediated membrane fusion by anti-gHgL antibodies

Karthik Sathiyamoorthy[a], Jiansen Jiang[b,c], Britta S. Möhl[d,1], Jia Chen[d], Z. Hong Zhou[b,c], Richard Longnecker[d], and Theodore S. Jardetzky[a,2]

[a]Department of Structural Biology, Stanford University School of Medicine, Stanford, CA 94305; [b]Department of Microbiology, Immunology, and Molecular Genetics, University of California, Los Angeles, CA 90095; [c]California NanoSystems Institute, University of California, Los Angeles, CA 90095; and [d]Department of Microbiology and Immunology, Feinberg School of Medicine, Northwestern University, Chicago, IL 60611

Herpesvirus entry into cells requires the coordinated action of multiple virus envelope glycoproteins, including gH, gL, and gB. For EBV, the gp42 protein assembles into complexes with gHgL heterodimers and binds HLA class II to activate gB-mediated membrane fusion with B cells. EBV tropism is dictated by gp42 levels in the virion, as it inhibits entry into epithelial cells while promoting entry into B cells. The gHgL and gB proteins are targets of neutralizing antibodies and potential candidates for subunit vaccine development, but our understanding of their neutralizing epitopes and the mechanisms of inhibition remain relatively unexplored. Here we studied the structures and mechanisms of two anti-gHgL antibodies, CL40 and CL59, that block membrane fusion with both B cells and epithelial cells. We determined the structures of the CL40 and CL59 complexes with gHgL using X-ray crystallography and EM to identify their epitope locations. CL59 binds to the C-terminal domain IV of gH, while CL40 binds to a site occupied by the gp42 receptor binding domain. CL40 binding to gHgL/gp42 complexes is not blocked by gp42 and does not interfere with gp42 binding to HLA class II, indicating that its ability to block membrane fusion with B cells represents a defect in gB activation. These data indicate that anti-gHgL neutralizing antibodies can block gHgL-mediated activation of gB through different surface epitopes and mechanisms.

herpesvirus | EBV | membrane fusion | neutralizing antibody | glycoprotein complex

All enveloped viruses need to enter their host cells by membrane fusion before transferring their genetic information and establishing infection (1). Both envelope glycoproteins and bilayer membranes undergo progressive structural transitions that ultimately result in the opening of a fusion pore. Herpesviruses are dsDNA viruses with a large linear genome (hundreds of kilobases) packed into an icosahedral capsid surrounded by tegument and enveloped within a lipid membrane with embedded glycoproteins that mediate entry. Herpesviruses require two glycoprotein complexes, a gHgL heterodimer and a gB homotrimer, for entry into all host cell types. gB is thought to drive membrane fusion through conformational changes, while gHgL is thought to regulate gB activation (2–4). Apart from being mechanistically important for entry, both gB and gHgL are targets of neutralizing antibodies (5), highlighting their potential as subunit vaccine antigens (6, 7). In addition to these core fusion proteins, other nonconserved proteins encoded by herpesviruses can recognize specific host cellular receptors, triggering membrane fusion and establishing viral tropism. This involvement of multiple viral glycoproteins in cell targeting and membrane fusion activation is a hallmark of the herpesviruses; however, the interactions and roles of the component glycoproteins are still incompletely understood.

Herpesviruses are divided into three subfamilies: *Alphaherpesvirinae*, *Betaherpesvirinae*, and *Gammaherpesvirinae*. Nine members of this family infect humans and thus are termed human herpesviruses (HHVs). The prototypical gamma-herpesvirus Epstein-Barr virus (EBV, or HHV-4) is the etiologic agent for acute infectious mononucleosis in children and young adults. Predominantly in immunocompromised patients, EBV also has been causally associated with Burkitt and Hodgkin lymphoma, T/natural killer cell lymphoproliferative disorders, and epithelial cell disorders such as nasopharyngeal carcinoma and certain gastric carcinomas. These secondary diseases highlight the two predominant host cells targeted for EBV infection, B cells and epithelial cells, with life-long latency established in B cells (2, 3).

EBV entry into epithelial or B cells is thought to involve sequential activation of gHgL through interactions with different cellular receptors, followed by activation of gB. gB belongs to the class III fusion proteins, which includes baculovirus gp64 and vesicular stomatitis virus (VSV) G (8, 9). Both EBV entry pathways share the common requirement for gB as the fusogen to catalyze entry (10, 11), but how gB is activated by gHgL receptor binding remains poorly understood. gHgL binds either directly to a receptor for epithelial cell entry (12) or indirectly to HLA class II through a complex formed with the gp42 protein. EBV gp42 binds tightly to gH mainly through its N domain and to HLA class II (13–15) through its C domain. Because gp42 inhibits entry into epithelial cells, through interactions localized to its N domain, it acts as a tropism switch (16). High levels of gHgL/gp42 complexes in virions promote infection with B cells, while inhibiting epithelial cell entry (17). Correspondingly, high levels of gHgL lacking gp42 favor infection of epithelial cells. This inhibitory action of gp42 can be recapitulated by short gp42 N-domain peptides (residues 33–85), which bind tightly with nanomolar potency (18, 19) to gH. Additional EBV protein interactions,

such as gp350/220 binding to complement receptor 2 (CR2 or CD21) (20) or CD35 (21), and BMRF2 (22) binding to integrins (β1 integrin and α5 integrin), increase the efficiency of B-cell and epithelial cell fusion while themselves being dispensable for fusion.

The structures of many components of the herpesvirus entry machinery have been determined. The presumed postfusion crystal structures of herpes simplex virus 1 (HSV-1) (23), EBV (24), and cytomegalovirus (CMV) (25, 26) gB have been solved, showing largely similar architecture but different orientations of individual domains, surface charge states, and glycosylation patterns, likely pointing to differences in virus-specific entry. gB has overall similarities to VSV G and baculovirus gp64 (other class III fusogens), with VSV G serving as an important structural guide. VSV G alone has been solved in two structural states thought to correspond to prefusion (27) and postfusion (28) conformations. Similarities of postfusion gB with VSV G suggest that a large conformational change as observed for VSV G is needed to drive membrane fusion. However, VSV G is a pH-activated fusion protein, does not require a gHgL equivalent, and is not as large as gB (approximately 500 aa for VSV G, compared with 900 aa for herpesvirus gB). While a detailed herpesvirus prefusion gB structure has been elusive, a recent subtomogram-averaging model of a compact form of HSV gB in vesicles provided a model of a low-resolution, partial "pre-postfusion" gB structure with its fusion loops splayed 5 nm apart and pointed away from its transmembrane region (29).

Crystal structures of the ectodomain of HSV-2 (30), varicella-zoster virus (31), pseudorabies virus (32), and EBV (33) gHgL have been solved and show a strikingly similar boot-shaped (HSV, varicella-zoster virus) or rod-shaped (EBV) conformation with sequentially arranged four domains (D-I to D-IV). A recent structure of CMV gHgL as part of a pentamer shows a close resemblance to EBV gHgL (34). Unlike EBV, the CMV gHgL D-I/D-II is rotated and does not exhibit a prominent groove, with the overall shape and interdomain angles in between those of HSV-2 and EBV gHgL. Mutations within gHgL that affect fusion function are found throughout the length of the molecule, especially in D-I, the D-I/D-II interface, and D-IV for EBV (35–39), highlighting the importance of gHgL in fusion and surfaces of gHgL that differentially impact entry to different host cells. EBV gHgL contains a prominent loop in D-II with a KGD (lysine, glycine, aspartic acid) motif implicated in binding to integrins. Gp42 crystal structures of its C domain with (15) and without HLA class II (40) highlight the slight widening of an exposed surface, functional for B-cell fusion (41), the so-called hydrophobic pocket (HP), which may be the trigger for activating B-cell entry (10). We recently determined the structure of a complete gHgL/gp42 complex, revealing that the gp42 N-domain wraps around three gH domains, tethering its C-terminal receptor-binding domain to the complex (42). The C-domain HP forms a secondary interface with gH at its D-II (10) near the surface-exposed KGD motif region (35). EM analysis of a reconstituted B-cell triggering complex consisting of gHgL, gp42, and HLA class II indicates that the gp42 HP interaction with gH may be important for stabilizing a "closed" conformation that could promote closer approach of the viral and cellular bilayers (10). The mechanism by which receptor binding provides signals for gB activation remains unclear, however.

Anti-gHgL antibodies have been shown to be potent inhibitors of herpesvirus entry and provide tools for investigating mechanistic features of the entry machinery and pathway. Anti-gHgL antibodies could block membrane fusion and virus entry by directly blocking interactions with host cell receptors or gB, but they could also interfere with other obligate gHgL activities or structures necessary for membrane fusion to proceed. We previously solved the structure of the anti-gHgL antibody E1D1 in complex with gHgL/gp42, demonstrating that it engages gL residues at the tip of D-I (42). E1D1 partially blocks membrane fusion with epithelial cells, but not B cells, and gL residues located within or near the

epitope show a similar epithelial cell-specific modulation of fusion (42).

Here we have extended these studies to investigate the anti-gHgL CL40 and CL59 antibodies, which inhibit fusion with both epithelial and B cells. We mapped the epitopes of CL40 and CL59 using X-ray crystallography and electron microscopy, respectively. The three anti-gHgL mAbs have nonoverlapping epitopes and engage distinct functional regions of EBV gHgL, revealing different functional profiles in blocking membrane fusion. CL59 binds an epitope in gH D-IV, proximal to the viral membrane and distant from known receptor binding sites, indicating the functional importance of this domain in fusion activation. CL40 binds to an epitope in gH D-II that overlaps substantially with a region observed to interact with the gp42 HP. However, CL40 binds with similar affinity to gHgL and the gHgL/gp42 complex, consistent with its ability to inhibit membrane fusion with B cells. Surface plasmon resonance (SPR) binding studies have shown that CL40 also does not block the binding of gHgL/gp42 complexes to HLA, indicating that its inhibition of membrane fusion with B cells is not due to an interference with receptor binding. CL40 inhibition may perturb the overall architecture of the gHgL/gp42/HLA triggering complex by displacing gp42, thereby blocking activation of gB-mediated fusion. Overall, our findings indicate that anti-gHgL antibodies can block virus entry through distinct mechanisms and epitopes, interfering with intermediate steps along the membrane fusion pathway to block the activation or the efficiency of gB-mediated membrane fusion.

Results

CL40 and CL59 Antibodies Show Different Abilities to Inhibit Membrane Fusion as Intact mAbs vs. Fabs.
Previous studies have demonstrated that the CL40 and CL59 antibodies neutralize EBV infection of both B cells and epithelial cells (43). To examine the effects of the CL40 and CL59 Fabs, we purified to homogeneity both Fab fragments and tested them in a luciferase-based cell–cell fusion assay. We observed that both CL40 and CL59 mAbs potently blocked membrane fusion with epithelial and B cells (Fig. 1 *A–D*), consistent with previous studies. However, while the CL40 Fab retained the ability to inhibit fusion with both cell types (Fig. 1 *A* and *B*), the CL59 Fab was noninhibitory at all concentrations tested (Fig. 1 *C* and *D*). Titrations of the mAbs and Fabs showed that the CL40 mAb was more potent than Fab in reducing activity (Fig. 1 *A* and *B*). In contrast, the CL59 Fab showed minimal inhibition of cell fusion at up to 250 nM, indicating that the inhibitory activity is significantly dependent on the intact dimeric mAb. The experiment was repeated in triplicates with 200 nM of final antibody concentration (Fig. 1 *E* and *F*), yielding similar results.

Because previous studies indicated that CL59 Fab could inhibit EBV infection (43), we conducted neutralization experiments with epithelial cells using an EBV-GFP reporter virus and purified CL40 and CL59 Fabs (Fig. S1). Fluorescence images obtained at 24 h postinfection and flow cytometry cell counts showed that both Fabs inhibit virus entry. CL40 Fab inhibition of cell–cell fusion and EBV infection exhibited similar concentration dependence. In contrast, CL59 Fab exhibited ∼50% inhibition of EBV infection at 150 nM CL59 Fab, where no inhibition of cell–cell membrane fusion was observed. These data suggest that the CL59 inhibition of cell–cell fusion may require a greater level of saturation of the cell surface gHgL compared with the levels needed to inhibit EBV virions.

Binding Affinities and Kinetics of CL40 and CL59 Fabs to gHgL and gHgL/gp42 Complexes.
The interaction of gp42 with gHgL involves an extensive interface between the gp42 N-terminal domain that includes interactions extending over multiple gH domains (D-II to D-IV), which could affect antibody epitopes and binding affinity (42). Previous studies indicated that CL59 binds to an epitope located in gH D-IV, while an epitope for CL40 had not
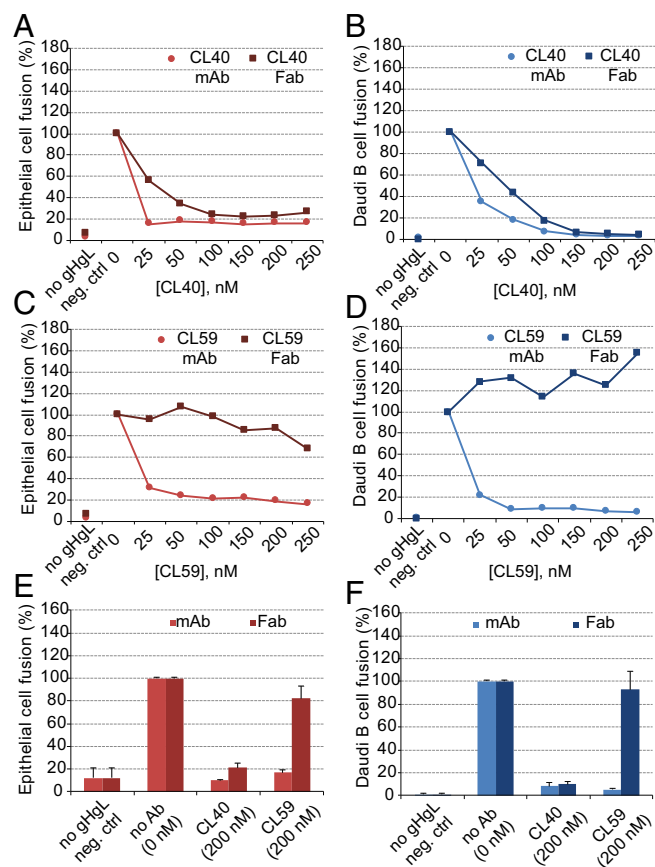
Fig. 1. CL40 and CL59 inhibition of membrane fusion. (*A* and *B*) Inhibition of fusion activity with purified CL40 mAb (lighter color shade) and Fab (darker color shade) using epithelial cells (*A*) and B cells (*B*). (*C* and *D*) Inhibition of fusion activity with purified CL59 mAb (lighter color shade) and Fab (darker color shade) using epithelial cells (*C*) and B cells (*D*). For these panels, the x-axis indicates the amount of purified antibody as final concentration in nanomoles. Empty pSG5 plasmid with no gH or gL insert serves as the negative control, and fusion activity with no antibody is set to 100% for HEK 293 epithelial cells (maroon) and Daudi B cells (blue). Each data point is represented by a single experiment titrating the antibody (except negative control). (*E* and *F*) Fusion activity expressed as the average from three independent experiments (biological replicates) with a 200 nM final antibody concentration, with fusion activity expressed as percentage with WT and no antibody data point set at 100% for HEK 293 epithelial cells (*E*) and Daudi B cells (*F*). In each experiment, the negative control is pSG5 plasmid with no gH or gL insert.

been mapped in gH (38, 39). To examine the affinities of the CL40 and CL59 Fabs for gHgL, and the potential effect of gp42 on their binding, we conducted SPR binding studies. Purified gHgL (Fig. 2 *A* and *C*) or gHgL/gp42 complexes (Fig. 2 *B* and *D*) were immobilized as ligands and exposed to increasing concentrations of CL40 or CL59 Fabs. The resulting sensorgram data were fit to a global 1:1 interaction model (Fig. 2 *A–D*), and association rate (k_a), dissociation rate (k_d), and dissociation constant (K_D) were calculated (Table 1). Both CL40 and CL59 Fabs bound gHgL with nM potency and with equilibrium K_D values of 29 nM and 156 nM, respectively. The presence of gp42 bound to gHgL had little effect on the interaction of the CL40 and CL59 Fabs (Table 1). The CL59 K_D value remained unchanged in the presence of gp42, while the CL40 K_D value for the gHgL/gp42 complex was approximately twofold that of gHgL affinity (Table 1). We note that that this difference in K_D values is due primarily to a slower association rate of CL40 Fab with gHgL in the presence of gp42.

Our SPR analysis of CL40 binding affinity is consistent with its inhibition in the cell–cell fusion assay (Fig. 2*A*). CL40 concentrations of 25–50 nM, similar to its K_D values of 30–68 nM, inhibited membrane fusion with B cells in the 40–60% range. These data indicate that CL40 occupancy of its epitope on either gHgL or gHgL/gp42 is sufficient to block gHgL-mediated fusion. In contrast, CL59 Fab concentrations of up to 250 nM, which exceed its K_D value, showed little to no inhibition of gHgL in the fusion assays (Figs. 1 *C* and *D* and 2*B*). The ability of both CL40 and CL59 Fabs to form stable complexes with gHgL/gp42 was confirmed by gel filtration chromatography (Fig. 2 *E* and *F*). These data further indicate an epitope-specific difference in the inhibitory activities of the CL40 and CL59 mAbs.

The Crystal Structure of CL40 Bound to gHgL. To understand the structural basis for CL40 and CL59 inhibition of gHgL, we performed crystallization and EM studies of complexes of the antibody Fabs with gHgL. The CL40 and CL59 Fabs were incubated
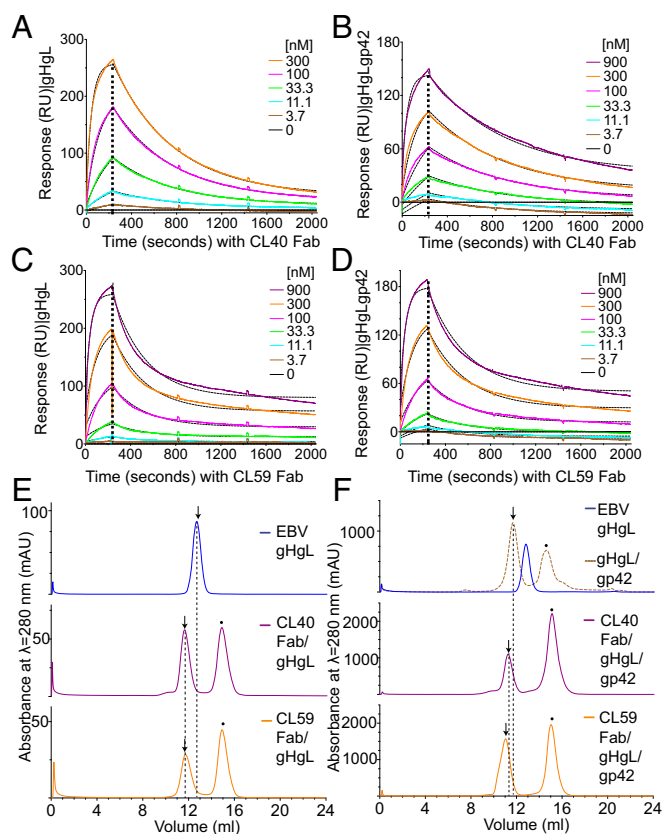
Fig. 2. CL40 and CL59 bind to both gHgL and gHgL/gp42 complexes. (*A* and *B*) CL40 Fab ("analyte") binding sensorgram curves showing association and dissociation phases for a concentration series with immobilized gHgL (ligand) (*A*) and with immobilized preformed gHgL/gp42 (ligand) (*B*). (*C* and *D*) CL59 Fab (analyte) binding sensorgram curves showing association and dissociation phases for a concentration series with immobilized gHgL (ligand) (*C*) and immobilized preformed gHgL/gp42 (ligand) (*D*). The 1:1 global fit of the curves is overlaid as black dashed curves (using GraphPad Prism). Kinetic parameters calculated from a 1:1 model fit are collected in Table 1. (*E*) Gel filtration chromatograms showing the assembly of distinct complexes of CL40Fab and CL59Fab with gHgL from individually purified proteins. (*F*) Gel filtration chromatograms showing the assembly of distinct complexes of CL40Fab and CL59Fab with gHgL/gp42 from individually purified proteins. In *E* and *F*, the shift in elution volume (Ve) indicative of additive formation of complex is highlighted by vertical dashed lines. The arrow denotes the complex of interest, and the black dot at the top of the peak denotes excess Fab or gp42.

Table 1. SPR kinetic parameters from a 1:1 interaction model

Stationary phase (ligand)	Surface density of ligand, RU*	Mobile phase (analyte)	k_a, M^{-1} · s^{-1} (×10^3)	k_d, s^{-1} (×10^{-3})	K_D, nM
gHgL	1,780	CL40 Fab	64.51	1.88	29.1
gHgL/gp42	1,110	CL40 Fab	22.02	1.51	68.8
gHgL	1,780	CL59 Fab	21.94	3.42	156.1
gHgL/gp42	1,110	CL59 Fab	20.14	2.94	145.8
HLA-DQ2 (α1)	750	gHgL/gp42	178.52	27.77	155.6
HLA-DQ2 (α1)	750	CL40/gHgL/gp42	709.91	22.67	31.9

*Ligand density rounded off to the nearest tenth after subtracting RU value of baseline level after a deactivation step with ethanolamine for the ligand channel minus the corresponding reference channel (Ch4-Ch1 or Ch3-Ch2).

with purified gHgL/gp42 complex or gHgL bound to a gp42-derived peptide (gp42; aa 47–81) and isolated by gel filtration chromatography (Fig. 2 E and F and Fig. S2A). Negative-stain EM images of the purified complexes provided further evidence of the homogeneity and integrity of the anti-gHgL Fab complexes (Fig. S3). Crystallization conditions were identified for the CL40/gHgL/gp42 (47–81) complex (Fig. S2B), and optimized crystals were obtained (Fig. S2B, green box) that diffracted synchrotron X-rays to ∼3 Å. The crystal diffraction was anisotropic and corrected by ellipsoid truncation of the unmerged reflections using the diffraction anisotropy server (44), providing resolution limits along the three crystallographic axes: a* = 3.6 Å, b* = 2.9 Å, c* = 3.0 Å. The CL40 sequence was obtained by sequencing cDNA isolated from the CL40 hybridoma cells (a generous gift from Lindsey Hutt-Fletcher) (Fig. S4A). We found two CL40/gHgL/gp42(47–81) complexes in the asymmetric unit, with no crystal contacts in gH D-IV, and poor electron density relative to other regions of the final model. The final refinement yielded an R/R_{free} ratio of 0.25/0.29, with overall good model geometry (Table S1).

The crystal structure of the CL40/gHgL/gp42(47–81) complex revealed that the Fab binds an epitope located at the gH D-II/D-III interface of gH (Fig. 3A) and does not contact the gp42 N-domain peptide present in the complex. There are no noticeable conformational changes in either gHgL or the gp42 N-domain residues (47–81) present in the complex. CL40 interacts predominantly with gH D-II using light chain contacts composed of L-CDR3 with the N-terminal end of gH:2α-7 (helix 7 in gH:D-II), and L-CDR1 with the loop connecting gH:2α-4 and gH:2α-5. Key residue interactions include hydrogen bonds (H-bonds) between gH:D284 and L-CDR3:Y94, gH:E286 and L-CDR3:N92, and the backbone of gH:V243 and L-CDR1:N32. There is also minimal lateral contact with gH D-III between L-CDR1:Q27 and the C-terminal end of gH:3α-6, and V_L:D1 with gH:N508 on the other side. CL40 heavy chain contacts with gH include H-CDR2:D52 and H-CDR2:D55, forming salt bridges with gH:R184, and backbone H-bonds between H-CDR3:L100 and H-CDR3:L101 with gH:H239 (Fig. 3B).

The CL40 Epitope Overlaps with the Site of the gp42 C-Domain Interaction of gH. The CL40 footprint on gH overlaps substantially with the interaction site formed between the gp42 C-domain and gH observed in our previous structure of the gHgL/gp42 complex

(Fig. 4 A–C). The gp42 C-domain interaction is of weak affinity, involving one edge of a hydrophobic pocket (HP) of the gp42 C-type lectin domain (CTLD). Three out of four gH loops involved in gH binding with gp42 HP, between helices 2α-4 and 2α-5, helices 2α-6 and 2α-7, and β strands 2β-6 and 2β-7, also interact with CL40 CDRs. Although CL40 and gp42 share this interaction site on gH, gp42 does not significantly inhibit CL40 binding to gH, although our SPR data indicate that its presence may slightly interfere with CL40 association (Table 1). The overlap between CL40 and gp42 sites with gH was also directly visualized in negative-stain EM 2D class averages of CL40 bound to gHgL/gp42 complexes (10) (Fig. 4D and Fig. S5A). The 2D classes of CL40/gHgL/gp42 complex reveal all the component proteins as identified by their size and relative shape while being consistent with the crystal structure (Fig. 4D).

Both the EM and the crystal structure data indicate that CL40 Fab could potentially displace the gp42 C-domain from its interaction site with gH without dissociating gp42 from the complex. To test whether the binding of CL40 could interfere with HLA class II binding, and thereby inhibit membrane fusion with B cells, we performed SPR binding studies between immobilized HLA-DQ2 and the gHgL/gp42 or CL40/gHgL/gp42 complex (Fig. 4 E and F). Both complexes bound to HLA-DQ2, with the CL40 complex exhibiting a higher-affinity interaction with HLA-DQ2, indicating that CL40 does not block HLA binding. These results suggest that CL40-mediated inhibition of B-cell fusion may involve a perturbation of the architecture of the gHgL/gp42 complex. This may parallel the effects of gp42 mutations within the HP, which also inhibit membrane fusion and have been observed to alter the conformational distribution of "open" and closed states of the gHgL/gp42/HLA "triggering complex."

A Pseudoatomic Model of CL59 Bound to gHgL Maps Its Epitope Within C-Terminal gH Domains. We mapped the interaction of CL59 with gHgL by generating a 3D reconstruction of gHgL complexes using negative-stain EM images (Fig. 5A). Since the gHgL protein has limited features at low resolution that can be used to identify its orientation, we generated complexes of CL59 with gHgL in the presence of the CL40 and E1D1 Fabs for which we have independent crystal structures. These complexes provide greater orientation constraints on generating a pseudoatomic model for the CL59 interaction to establish its epitope location (Fig. 5 B and C).

The model of the CL59/E1D1/CL40/gHgL/gp42(47–81) complex shows that CL59 binds to the back side of gH D-III/D-IV close to gH D-III residues 494–503 (loop between 3α-8 and 3α-9), 456–468 (3α-6 helix), and 406–415 (loop between 3α-3 and 3α-4), and gH D-IV loop residues 645–656 (loop between 4α-1 and 4β-9), 623–626 (loop between 4β-7 and 4β-8), and 568–577 (loop between 4β-3 and 4β-4) (Fig. 5C). In contrast to CL40, the binding of CL59 Fab to its epitope does not effectively inhibit cell–cell membrane fusion, despite the potent inhibitory activity of the intact mAb. These data indicate that inhibitory antibodies

Table 2. SPR steady-state analysis to derive K_D

Stationary phase (ligand)	Surface density of ligand, RU*	Mobile phase (analyte)	R_{max}	K_D, nM
HLA-DQ2 (α1)	750	gHgL/gp42	79.6	134.6
HLA-DQ2 (α1)	750	CL40/gHgL/gp42	63.7	45.1

*Ligand density rounded off to the nearest tenth after subtracting RU value of baseline level after a deactivation step with ethanolamine for the ligand channel minus the corresponding reference channel (Ch4-Ch1 or Ch3-Ch2).
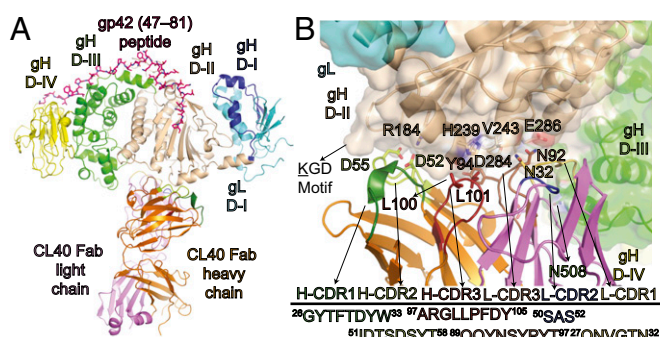
Fig. 3. Crystal structure of CL40 bound to gHgL/gp42. (*A*) Structure overview in a cartoon representation with gL in cyan, gH D-I in blue, D-II in wheat, D-III in green, D-IV in yellow, gp42(47–81) shown as sticks in hot pink, CL40Fab heavy chain in orange, and CL40Fab light chain in purple. (*B*) Close-up view of CL40 CDR interfaces with gH D-II and D-III showing overlap with the gp42 CTLD-binding region. Predominant side chain-specific interactions are CL40V$_H$:D52 and CL40V$_H$:D55 from H-CDR2 with gH:R184 and CL40V$_L$:N92 from L-CDR3 with gH:E286. The sequences for H-CDR1 (green), H-CDR2 (yellow), H-CDR3 (brick red), L-CDR1 (dark yellow), L-CDR2 (blue), and L-CDR3 (brown) are shown at the bottom below the solid black line. A complete CL40 Fab sequence is shown in Fig. S4. Structures were rendered using MacPyMol.

can engage different surfaces of gHgL, mediating inhibition through distinct mechanisms that likely interfere with the activation of gB-mediated membrane fusion.

Discussion

Herpesvirus entry into cells is a complex process involving coordinated actions of multiple viral glycoproteins, including the core membrane fusion machinery composed of gHgL and gB glycoproteins. Here we studied two anti-gHgL antibodies, CL40 and CL59, that potently block EBV-mediated membrane fusion with both B cells and epithelial cells. We observed that CL40 retains its inhibitory activity as a monomeric Fab, with potency consistent with its binding affinity for gHgL and gHgL/gp42 complexes. In contrast, CL59 Fab loses the ability to block membrane fusion with both cells even at concentrations exceeding its apparent K_D value for gHgL.

The X-ray and EM structures of the CL40 and CL59 complexes with gHgL map their respective epitopes. CL40 binds to a gH site that is also involved in interactions with the gp42 C-domain. We previously proposed that interactions between the gp42 C-domain and gH at this site are necessary for membrane fusion activity (10), possibly by stabilizing a closed conformation of gHgL/gp42/HLA triggering complexes (Fig. 6*A*). CL40 may displace the gp42 C-domain at this site, disrupting the overall architecture of the complex and thereby blocking activation of gB. Our crystal structure further suggests that CL40 could inhibit epithelial cell fusion by blocking epithelial cell receptor interactions, although we have not been able to observe direct gHgL-integrin binding to test this possibility. In contrast, the EM structure of the CL59 complex shows that its epitope is on a lateral side of D-IV predicted to be proximal to the viral membrane surface.

The CL59 Fab exhibited disparate inhibitory activities on cell-based membrane fusion and EBV infection, indicating that virions are more susceptible to inhibition. Our structural results show that CL59 does not bind close to known receptor binding sites on gHgL, consistent with a steric mechanism that could possibly block interactions with and activation of gB. Thus, both CL40 and CL59 appear to inhibit EBV-mediated membrane fusion by trapping nonfunctional intermediates along the pathway of gB activation (Fig. 6 *A* and *B*). At present, it is not possible to determine whether gB activation can occur in the presence of these

inhibitory antibodies but is nonproductive, or whether gB activation is fully blocked.

Anti-gHgL antibodies may provide potent immunity to herpesvirus infection, and gHgL complexes are potential targets for subunit vaccine development. For example, human CMV (HCMV) assembles multiple distinct gHgL complexes that are required for virus entry into fibroblast, epithelial, endothelial, and myeloid cells. HCMV gHgL forms pentameric complexes with the UL128, UL130, and UL131 proteins and a separate trimeric complex with the gO protein. The gHgL pentamer is essential for the virus to enter epithelial, endothelial, and myeloid cells and is also the target of particularly potent neutralizing antibodies. The overall architecture of HCMV gHgL complexes (45) and their interactions with a panel of neutralizing Abs (nAbs) (46) have been studied using EM. Our studies of the E1D1, CL40, and CL59 antibodies to EBV gHgL have identified interesting parallels with anti-HCMV gHgL mAbs. A comparison of recent HCMV pentamer:nAb structures (34) with EBV gHgL complexes shows similar epitope locations for CL40 and CL59 with two anti-HCMV antibodies (13H11 and 3G16; Fig. 6*C* and Fig. S6). These observations identify gHgL regions that are functionally important in both betaherpesvirus and gammaherpesvirus entry, suggesting common mechanisms of membrane fusion activation as well as the therapeutic potential of targeting gHgL for vaccine development for different herpesviruses.

Methods

Protein Expression and Purification. EBV gHgL and gp42 were produced in insect cells and purified as described previously (10). In brief, baculovirus stocks with the target protein gene of interest were used to infect 1.8 million cells/mL of insect cells, grown under shaking at 135 rpm at 27 °C for 3 d. Clarified supernatant was then passed through affinity columns for purification, using an E1D1 antibody column for gHgL and metal affinity (Ni^{2+}- or Co^{2+}-based resin) for gp42. Gp42 N-domain peptide (residues 47–81) was chemically synthesized by EZBiolab to 97.5% purity and resuspended in 20 mM Tris and 150 mM NaCl, pH 7.4 buffer at a stock concentration of 11 mg/mL. Soluble HLA-DQ2 (with α1 gliadin peptide) was purified from stable *Drosophila* S2 cells as described previously (10). Anti-gHgL mAb-expressing hybridoma cells (CL40, E1D1, and CL59) were a generous gift from Lindsey Hutt-Fletcher. The cells were amplified by the National Cell Culture Center (NCCC/Biovest) and individual mAbs purified by protein G resin in house from the clarified supernatants. All proteins were stored in final gel filtration (S200) buffer, 20 mM Tris, and 150 mM NaCl, pH 7.4.

Fab Production from Purified Anti-gHgL mAbs. For functional, crystallographic, and EM studies, the E1D1, CL59 (both IgG2a subclass), and CL40 (IgG1 subclass) mAbs were enzymatically digested by papain (from papaya latex, P3125-25MG; Sigma-Aldrich) as described previously for E1D1 (42). In brief, papain digestion of anti-gHgL mAbs was carried out at 1:5 wt/wt ratio (excess mAb), with antibody exchanged into 0.1 M sodium citrate pH 6.0, 10 mM EDTA, and 10 mM cysteine. HCl (freshly made) for the digestion step. Fab fragments were generated with an overnight digestion (16 h) at 37 °C, followed by separation of the undigested, Fab, and Fc fragments by protein A resin (in 1× PBS pH 7.4) and gel filtration chromatography (Superdex 200; GE Life Sciences).

Cell-Based Fusion Assay in the Presence of Anti-gHgL Abs. Virus free cell-cell fusion assays with mAbs were performed as described previously (47). CHO-K1 cells (American Type Culture Collection CCL-61 or CRL-9618) served as the effector cells and were transfected with plasmids for luciferase (reporter gene) under T7 promoter control and with either gB and gHgL for measuring epithelial cell fusion activity or gB, gHgL, and gp42 for B-cell fusion activity. Wild-type protein fusion levels (positive control) in each experiment were set to 100%, and the effects of the added antibody were compared. At 16 h posttransfection using Lipofectamine 2000 (Invitrogen), the cells were washed, detached, counted, and mixed 1:1 with target cells stably expressing T7 RNA polymerase in the presence or absence of CL40 mAb, CL59 mAb or CL40 Fab, CL59 Fab. Target cells were either HEK-293-T14 cells to mimic epithelial cell fusion or Daudi-T7-29 cells for B-cell fusion, which stably express T7 RNA polymerase (41, 48).

The mixed cells were cultured in 24-well plates in Ham's F-12 medium with 10% heat inactivated FBS. After 24 h, the cells were washed with PBS and lysed
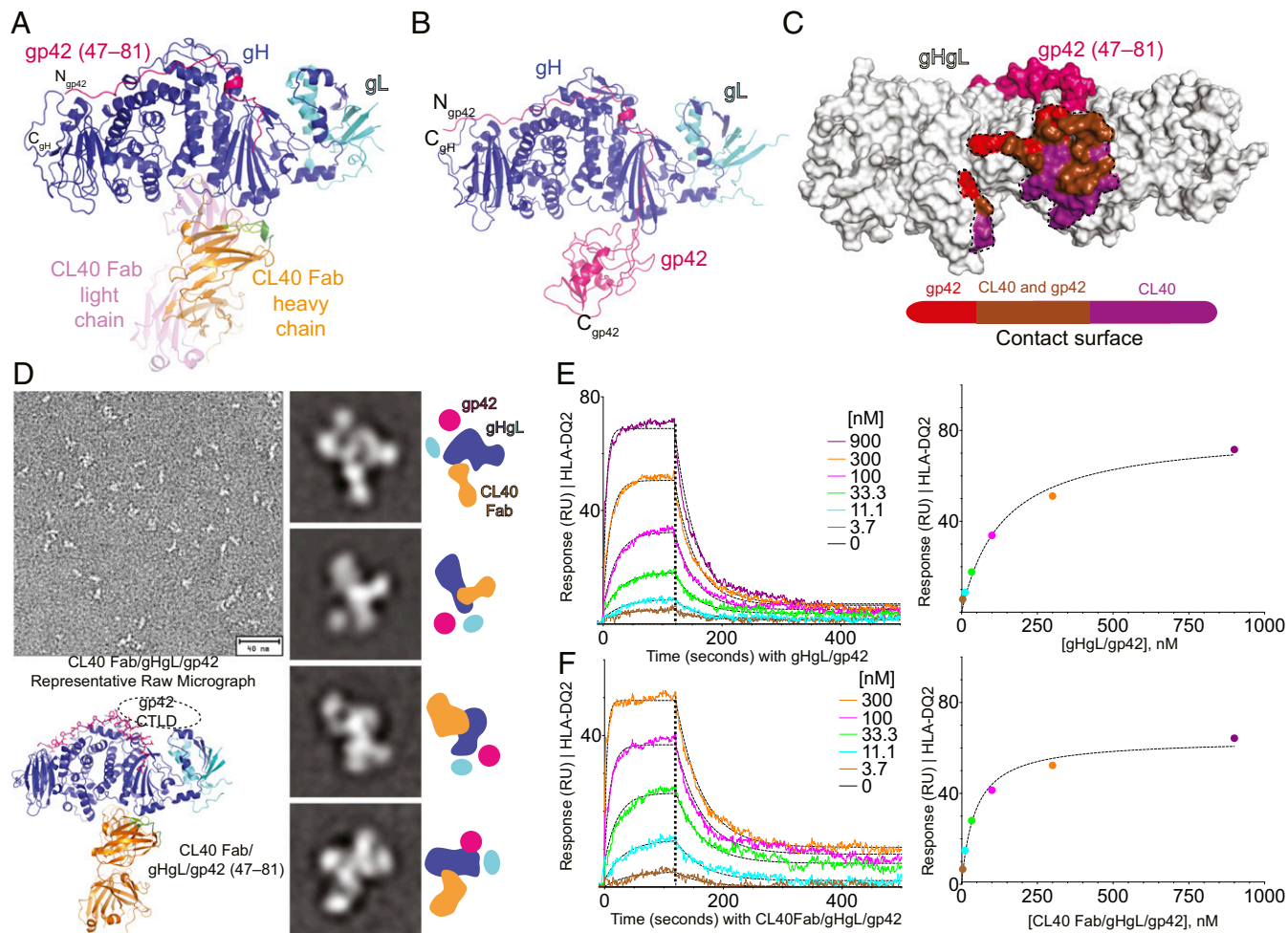
Fig. 4. CL40 binds a gH epitope that overlaps with the gp42 C-domain contact site. (*A* and *B*) Cartoon representations of the crystal structure of CL40Fab/gHgL/gp42(47–81) (*A*) and gHgL/gp42 complex (from PDB ID code 5T1D) (*B*) showing that the CL40 Fab binds to the same site on gH as the gp42 C-domain (CTLD). (*C*) The CL40 and gp42 C-domain CTLDs show substantial overlap in their respective surface contacts on gH. (*D*) Negative-stain EM of CL40Fab/gHgL/gp42 with a representative raw micrograph and selected 2D class averages showing the identity of all glycoproteins in the complex. All 250 2D class averages are shown in Fig. S5A. For each set of 2D class average showing a different view, a cartoon schematic at the side illustrates the identities of all component glycoproteins by their unique shape and size characteristics. The crystal structure of CL40 Fab/gHgL/gp42(47–81) is also shown for comparison. A dashed oval depicts the space occupied by the gp42 C-domain. The exaggerated movement of the gp42 C-domain perceived here could have resulted from flattening on the EM grid, while the actual displacement of gp42 C-domain could be small. (Scale bars: *Top Left*, 40 nm; *Middle*, 19 × 19 nm.) (*E* and *F*) CL40 Fab binding to gHgL/gp42 complexes does not interfere with the binding of HLA-DQ2. HLA-DQ2 (α1 gliadin) was immobilized on a CMD 200m biosensor chip using amine-coupling chemistry. Association and dissociation kinetics for a gHgL/gp42 preformed complex (*E*) and a CL40/gHgL/gp42 preformed complex (*F*) are shown with a 1:1 global fit model overlaid on data and shown as dashed curve (*Left*) and a steady-state analysis binding curve plotting analyte concentration (nM) versus response (RU) (*Right*). The K_D values from the two analyses are comparable with each other, as shown in Tables 1 and 2. In addition, the K_D value for binding of the preformed gHgL/gp42 to immobilized HLA-DQ2 obtained here and shown in Table 1 is comparable to the value obtained by the BLI method using Octet RED96 reported previously (10).

with 100 μL of passive lysis buffer (Promega). Luciferase activity was quantified from 20 μL of lysed cells with 100 μL of luciferase assay reagent (Promega) in a 96-well plate on a PerkinElmer Victor plate reader. Experiments were carried out with a single endpoint for antibody titrations and in triplicate (biological replicates) using a fixed final antibody concentration of 200 nM.

EBV Infection Assay. Here 7.5×10^5 cells infected with EBfaV-GFP (recombinant EBV reporter virus expressing GFP) were grown in 100 mL RPMI with 10% FBS, penicillin-streptomycin, and 30 ng/mL 12-O-tetradecanoylphorbol-13-acetate (TPA) at 37 °C in 5% CO_2 for 4 d. The supernatant was collected by spin down at $1,000 \times g$ for 10 min, aliquoted in 1 mL, and frozen at −80 °C, or was centrifuged at $21,000 \times g$ for 30 min at 4 °C. The pellets were resuspended in 100 μL of 10% FBS in DMEM. On the second day, 5×10^4 HEK 293 cells/well were seeded on a 48-well plate and infected with 100 μL of EBV in 10% FBS-DMEM. Defined amounts of CL40 Fab or CL59 Fab were added, fluorescent microscopy images were captured after 24 h, and cell counts were measured by flow cytometry after 48 h (Fig. S1).

SPR Binding Kinetics. We performed binding kinetics assays to determine on-rate (k_a), off-rate (k_d), and dissociation constant (K_D) between gHgL or gHgL/gp42 and CL40 or CL59 Fabs using a BiOptix 404pi biosensor instrument, with 1× PBS pH 7.4 with 0.05% (vol/vol) Tween-20 as the running buffer. EBV gHgL and preformed gHgL/gp42 complex were separately immobilized as the "ligands" on two different channels (Ch3 and Ch4) of a carboxy-methyl dextrose (CMD) biosensor chip (200m; BiOptix) by the amine-coupling method using N-hydroxysuccinimide/1-ethyl-3-(3-dimethylaminopropyl)carbodiimide chemicals (Sigma-Aldrich). Each of the four flow cells in the Bioptix 404pi is 0.5 mm wide by 2 mm long with a height of 50 μ, and has a volume of 34 nL. As an approximation, 1 resonance unit (RU) of immobilized ligand is equivalent to 1 pg/mm². Both reference channel and blank injection subtracted sensorgrams with different serial dilutions (1:3) to generate a concentration series of the mobile analyte, either CL40 Fab or CL59 Fab, were obtained after passing over the immobilized ligand surface in a 2 × 2 kinetic mode. The resulting data were fit globally to a 1:1 interaction model using GraphPad Prism 7. Experiments on a separate CMD biosensor chip were carried out with soluble HLA-DQ2 (α1 gliadin peptide) as the immobilized ligand, using preformed gHgL/gp42 or CL40/gHgL/gp42
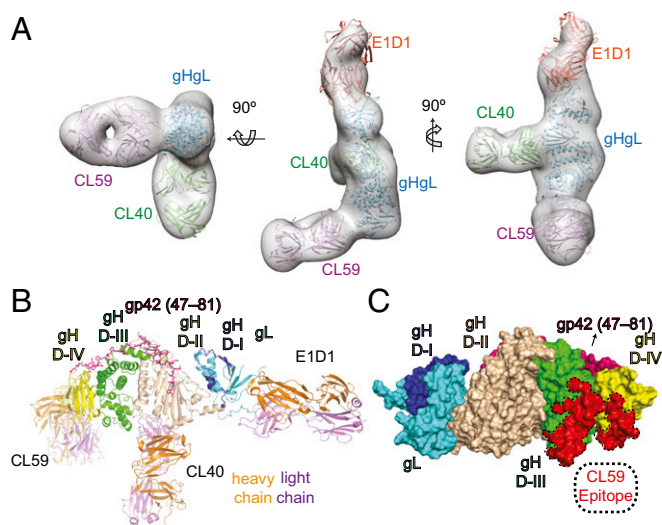
Fig. 5. CL59 binds to an epitope spanning gH domains D-III and D-IV. (*A*) 3D negative-stain EM model of three Fabs (CL59, CL40, and E1D1) bound to gHgL. The EM envelope (gray) is shown with fitted crystal structures of gHgL (blue) and three Fabs represented as CL59 Fab (purple), CL40 Fab (green), and E1D1 Fab (orange). The CL59 Fab shown here is based on a generic Fab model as there is no high resolution structure for CL59. The structure was rendered and fitted using UCSF Chimera. (*B*) Cartoon representation of the 3D reconstruction shown in *A*, with the heavy chain of each Fab shown in orange and the light chain shown in purple. gHgL is color-coded by individual domains: gL in cyan, gH D-I in blue, gH D-II in wheat, gH D-III in green, and gH D-IV in yellow. The model confirms that the three anti-gHgL Fabs have nonoverlapping epitopes on gHgL. (*C*) Surface mapping of the CL59 epitope on gH D-III/D-IV. Complete sequence and CDR assignments for CL40 and CL59 are shown in Fig. S4. The structures shown in *B* and *C* were rendered using MacPymol.

complex as the analyte. Kinetic parameters from the model fit are collected in Table 1, and reference subtracted sensorgram curves with the model fit curve overlaid (black dashes) on the data are shown in Figs. 2 *A*–*D* and 4 *E* and *F*. Steady-state analysis with HLA-DQ2 as the ligand also was performed to obtain a K_D measure that closely matches the K_D value derived from the kinetic fit model. In addition, the K_D value from gHgL/gp42 binding to HLA-DQ2 determined here by SPR closely matches the value obtained previously with the bio-layer interferometry (BLI) method using Octet RED96 (10).

Crystallization and Structure Determination of the CL40/gHgL/gp42(47–81) Complex. Individual glycoproteins were mixed on ice with limiting gHgL, incubated for 30 min, and then injected into a Superdex 200 gel filtration column to isolate the CL40/gHgL/gp42(47–81) complex for crystallization. The elution volume from S200 was 11.62 mL, corresponding to an apparent molecular weight of 178 kDa (Table S2). The final protein concentration was ≈6.4 mg/mL (protein A280 method with a NanoDrop spectrophotometer; Thermo Fisher Scientific) in 20 mM Tris and 150 mM NaCl, pH 7.4 buffer. Crystallization trials were done at room temperature (22 °C) using various sparse matrix and systematic screening kits (Qiagen and Hampton) with the Phoenix robot (Art Robbins Instruments). Multiple crystal hits were obtained (Fig. S2*B*). The best diffracting crystal initially grew as diamond-shaped stacked plates with the following reservoir condition: sodium sulfate/Bis-Tris propane/PEG 3350 [H8 condition in the pH-, anion-, and cation-testing (PACT) suite from Qiagen]. Optimized single crystals used for single-crystal X-ray diffraction experiments and structure solutions here grew in a 1:1 volume ratio of protein:reservoir with 0.25 M sodium sulfate, 0.1 M Bis-Tris propane pH 8.5, and 20% (wt/vol) PEG 4000 as the reservoir in a closed hanging-drop vapor diffusion system. Crystals appeared overnight and grew larger over a 2-wk period, when they were frozen and cryoprotected by a quick soak with corresponding mother liquor also containing 15% (vol/vol) PEG 400. Data collection was done at microfocus beamline 12–2 at the Stanford Synchrotron Radiation Laboratory in the SLAC National Accelerator Laboratory, and at beamline 21-ID-D (Life Sciences Collaborative Action Team) at the Advanced Photon Source (APS) of Argonne National Laboratory. The dataset used for structure solution here

was collected at beamline 21-ID-D with an overall anisotropic diffraction, with spots visible to approximately 3 Å.

The CL40/gHgL/gp42(47–81) structure was solved by molecular replacement (MR) with a single gHgL heterodimer [Protein Data Bank (PDB) ID code 3PHF] and Fab D6.3 (PDB ID code 2XQY) searching for two copies each in a single run of the Phaser search program (49). The number of search components was defined by the Matthews number calculation within ccp4 (50). Multiple different Fabs with different elbow angles and truncated complementarity-determining regions (CDRs) as prepared by the phenix.sculptor program (51, 52) were used for the MR search. MR confirmed the screw axes and defined the space group as $P2_12_12_1$. Difference maps (mFo-DFc) revealed a density corresponding to parts of the gp42(47–81) peptide. The electron density was improved by a single run of PHENIX AutoBuild. A polyalanine peptide was built in place of gp42(47–81), and the side chains were placed iteratively during refinement using phenix.refine.

Negative-Stain EM and Data Processing. EM grids covered with a thin layer of carbon film were rendered hydrophilic using glow discharge immediately before the experiments. In brief, 2 μL of purified sample was applied to a grid and then blotted with filter paper after a 30-s incubation, followed by staining with 0.8% uranyl formate. Negative-stain EM micrographs were recorded with a TIETZ F415MP 16-megapixel CCD camera at 50,000× nominal magnification on an FEI Tecnai F20 electron microscope operated at 200 kV. Micrographs were saved by 2× binning to yield a calibrated pixel size of 4.41 Å. Particles were automatically picked from micrographs using ApDogPicker.py in Appion (53) and then extracted into 80 × 80-pixel boxes. Phase flipping of contrast transfer function correction was performed on micrographs using the defocus values estimated by CTFFIND (54), and 2D classification was performed using refine2d.py in EMAN (55). For the CL40/gHgL/gp42 complex, a total of 180,000 particles picked from 296 micrographs were classified to generate 250 2D class
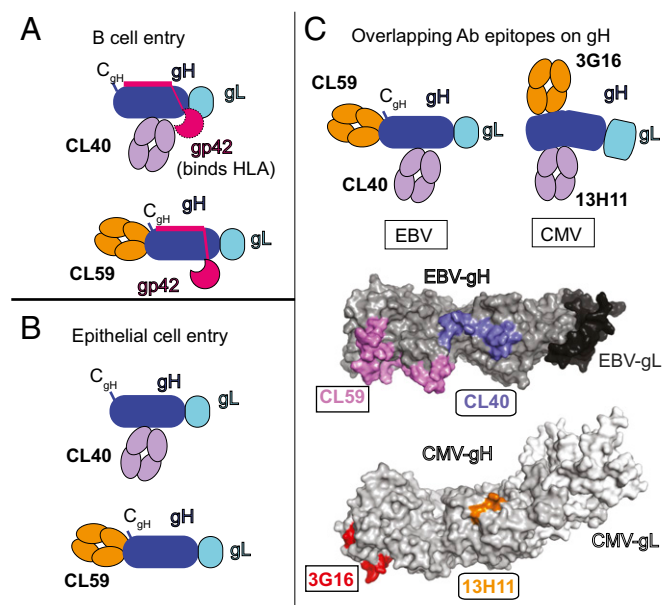
Fig. 6. CL40 and CL59 inhibition of membrane fusion and similarities in sites of vulnerability in EBV and CMV gHgL. (*A* and *B*) Schematic models for the inhibition of gHgL-mediated membrane fusion by CL40 and CL59 for B cells (*A*) and epithelial cells (*B*). CL40 likely disrupts the overall conformation of the entry triggering complex (gHgL/gp42/HLA class II) and its ability to activate gB. CL40 likewise could block interaction with the epithelial cell receptor, explaining its inhibition of epithelial cell fusion. CL59 engages an epitope in gH D-IV proximal to the viral membrane and distant from known receptor binding sites, likely acting by sterically blocking gB activation. (*C*) The CL40 and CL59 epitopes on EBV gHgL overlap the nAb epitopes in CMV gHgL, defined by 13H11 and 3G16, respectively. The crystal structures of EBV gHgL (from PDB ID code 5T1D) and CMV gHgL (from PDB ID code 5VOB) are shown in surface representation with the antibody epitopes as defined by crystal structure (for CL40), negative-stain EM (for CL59), and HDX-MS and negative-stain EM (for 3G16 and 13H11) as mapped and color-coded as in the figure.

averages. For the CL59/E1D1/CL40/gHgL/gp42(47–81) complex, 126,000 particles from 167 micrographs were classified into 100 classes, followed by visual inspection of 2D class averages to select a subset of 37,127 particles that have three Fabs bound to gHgL. This subset of particles was then used for 3D reconstruction and refinement using RELION (56). Since the 2D class averages of the CL59/E1D1/CL40/gHgL/gp42(47–81) complex suggested that the complex has an elongated shape, an artificial rod-shaped density (12 pixels in diameter and 45 pixels long) was used as an initial 3D model with low-pass filtering to 60 Å. The final resolution of 3D autorefinement was estimated as 16 Å (Fourier shell correlation, 0.143) using the RELION postprocess program (Fig. S5*B*).

Data Availability. The CL40/gHgL/gp42(47–81) coordinates and structure factors have been deposited in the PDB (ID code 5W0K). The DNA sequences of the CL40 and CL59 antibodies have been submitted to GenBank under accession nos. MF104552 (CL40 heavy chain), MF104553 (CL40 light chain), MF104554 (CL59 heavy chain), and MF104555 (CL59 light chain).

1. Harrison SC (2015) Viral membrane fusion. *Virology* 479–480:498–507.
2. Longnecker R, Kieff E, Cohen JI (2013) Epstein-Barr virus. *Fields Virology,* (Wolters Kluwer Health Adis (ESP), Philadelphia), 6th Ed, Vol 1.
3. Connolly SA, Jackson JO, Jardetzky TS, Longnecker R (2011) Fusing structure and function: A structural view of the herpesvirus entry machinery. *Nat Rev Microbiol* 9:369–381.
4. Chesnokova LS, Jiang R, Hutt-Fletcher LM (2015) Viral entry. *Curr Top Microbiol Immunol* 391:221–235.
5. Cui X, et al. (2016) Rabbits immunized with Epstein-Barr virus gH/gL or gB recombinant proteins elicit higher serum virus neutralizing activity than gp350. *Vaccine* 34:4050–4055.
6. Cohen JI, Fauci AS, Varmus H, Nabel GJ (2011) Epstein-Barr virus: An important vaccine target for cancer prevention. *Sci Transl Med* 3:107fs7.
7. Cohen JI (2015) Epstein-Barr virus vaccines. *Clin Transl Immunology* 4:e32.
8. Backovic M, Jardetzky TS (2009) Class III viral membrane fusion proteins. *Curr Opin Struct Biol* 19:189–196.
9. Baquero E, Albertini AA, Gaudin Y (2015) Recent mechanistic and structural insights on class III viral fusion glycoproteins. *Curr Opin Struct Biol* 33:52–60.
10. Sathiyamoorthy K, et al. (2014) Assembly and architecture of the EBV B cell entry triggering complex. *PLoS Pathog* 10:e1004309.
11. Möhl BS, Chen J, Sathiyamoorthy K, Jardetzky TS, Longnecker R (2016) Structural and mechanistic insights into the tropism of Epstein-Barr virus. *Mol Cells* 39:286–291.
12. Hutt-Fletcher LM, Chesnokova LS (2010) Integrins as triggers of Epstein-Barr virus fusion and epithelial cell infection. *Virulence* 1:395–398.
13. Li Q, et al. (1997) Epstein-Barr virus uses HLA class II as a cofactor for infection of B lymphocytes. *J Virol* 71:4657–4662.
14. Haan KM, Kwok WW, Longnecker R, Speck P (2000) Epstein-Barr virus entry utilizing HLA-DP or HLA-DQ as a coreceptor. *J Virol* 74:2451–2454.
15. Mullen MM, Haan KM, Longnecker R, Jardetzky TS (2002) Structure of the Epstein-Barr virus gp42 protein bound to the MHC class II receptor HLA-DR1. *Mol Cell* 9:375–385.
16. Borza CM, Hutt-Fletcher LM (2002) Alternate replication in B cells and epithelial cells switches tropism of Epstein-Barr virus. *Nat Med* 8:594–599.
17. Wang X, Kenyon WJ, Li Q, Müllberg J, Hutt-Fletcher LM (1998) Epstein-Barr virus uses different complexes of glycoproteins gH and gL to infect B lymphocytes and epithelial cells. *J Virol* 72:5552–5558.
18. Kirschner AN, Lowrey AS, Longnecker R, Jardetzky TS (2007) Binding-site interactions between Epstein-Barr virus fusion proteins gp42 and gH/gL reveal a peptide that inhibits both epithelial and B-cell membrane fusion. *J Virol* 81:9216–9229.
19. Liu F, Marquardt G, Kirschner AN, Longnecker R, Jardetzky TS (2010) Mapping the N-terminal residues of Epstein-Barr virus gp42 that bind gH/gL by using fluorescence polarization and cell-based fusion assays. *J Virol* 84:10375–10385.
20. Fingeroth JD, et al. (1984) Epstein-Barr virus receptor of human B lymphocytes is the C3d receptor CR2. *Proc Natl Acad Sci USA* 81:4510–4514.
21. Ogembo JG, et al. (2013) Human complement receptor type 1/CD35 is an Epstein-Barr virus receptor. *Cell Rep* 3:371–385.
22. Xiao J, Palefsky JM, Herrera R, Berline J, Tugizov SM (2008) The Epstein-Barr virus BMRF-2 protein facilitates virus attachment to oral epithelial cells. *Virology* 370:430–442.
23. Heldwein EE, et al. (2006) Crystal structure of glycoprotein B from herpes simplex virus 1. *Science* 313:217–220.
24. Backovic M, Longnecker R, Jardetzky TS (2009) Structure of a trimeric variant of the Epstein-Barr virus glycoprotein B. *Proc Natl Acad Sci USA* 106:2880–2885.
25. Chandramouli S, et al. (2015) Structure of HCMV glycoprotein B in the postfusion conformation bound to a neutralizing human antibody. *Nat Commun* 6:8176.
26. Burke HG, Heldwein EE (2015) Crystal structure of the human cytomegalovirus glycoprotein B. *PLoS Pathog* 11:e1005227.
27. Roche S, Rey FA, Gaudin Y, Bressanelli S (2007) Structure of the prefusion form of the vesicular stomatitis virus glycoprotein G. *Science* 315:843–848.
28. Roche S, Bressanelli S, Rey FA, Gaudin Y (2006) Crystal structure of the low-pH form of the vesicular stomatitis virus glycoprotein G. *Science* 313:187–191.
29. Zeev-Ben-Mordehai T, et al. (2016) Two distinct trimeric conformations of natively membrane-anchored full-length herpes simplex virus 1 glycoprotein B. *Proc Natl Acad Sci USA* 113:4176–4181.
30. Chowdary TK, et al. (2010) Crystal structure of the conserved herpesvirus fusion regulator complex gH-gL. *Nat Struct Mol Biol* 17:882–888.
31. Xing Y, et al. (2015) A site of varicella-zoster virus vulnerability identified by structural studies of neutralizing antibodies bound to the glycoprotein complex gHgL. *Proc Natl Acad Sci USA* 112:6056–6061.
32. Backovic M, et al. (2010) Structure of a core fragment of glycoprotein H from pseudorabies virus in complex with antibody. *Proc Natl Acad Sci USA* 107:22635–22640.
33. Matsuura H, Kirschner AN, Longnecker R, Jardetzky TS (2010) Crystal structure of the Epstein-Barr virus (EBV) glycoprotein H/glycoprotein L (gH/gL) complex. *Proc Natl Acad Sci USA* 107:22641–22646.
34. Chandramouli S, et al. (2017) Structural basis for potent antibody-mediated neutralization of human cytomegalovirus. *Sci Immunol* 2:eaan1457.
35. Chen J, Rowe CL, Jardetzky TS, Longnecker R (2012) The KGD motif of Epstein-Barr virus gH/gL is bifunctional, orchestrating infection of B cells and epithelial cells. *MBio* 3:e00290-11.
36. Chen J, Jardetzky TS, Longnecker R (2013) The large groove found in the gH/gL structure is an important functional domain for Epstein-Barr virus fusion. *J Virol* 87:3620–3627.
37. Möhl BS, Sathiyamoorthy K, Jardetzky TS, Longnecker R (2014) The conserved disulfide bond within domain II of Epstein-Barr virus gH has divergent roles in membrane fusion with epithelial cells and B cells. *J Virol* 88:13570–13579.
38. Wu L, Hutt-Fletcher LM (2007) Point mutations in EBV gH that abrogate or differentially affect B cell and epithelial cell fusion. *Virology* 363:148–155.
39. Wu L, Borza CM, Hutt-Fletcher LM (2005) Mutations of Epstein-Barr virus gH that are differentially able to support fusion with B cells or epithelial cells. *J Virol* 79:10923–10930.
40. Kirschner AN, Sorem J, Longnecker R, Jardetzky TS (2009) Structure of Epstein-Barr virus glycoprotein 42 suggests a mechanism for triggering receptor-activated virus entry. *Structure* 17:223–233.
41. Silva AL, Omerovic J, Jardetzky TS, Longnecker R (2004) Mutational analyses of Epstein-Barr virus glycoprotein 42 reveal functional domains not involved in receptor binding but required for membrane fusion. *J Virol* 78:5946–5956.
42. Sathiyamoorthy K, et al. (2016) Structural basis for Epstein-Barr virus host cell tropism mediated by gp42 and gHgL entry glycoproteins. *Nat Commun* 7:13557.
43. Chesnokova LS, Hutt-Fletcher LM (2011) Fusion of Epstein-Barr virus with epithelial cells can be triggered by αvβ6 in addition to αvβ5 and αvβ8, and integrin binding triggers a conformational change in glycoproteins gHgL. *J Virol* 85:13214–13223.
44. Strong M, et al. (2006) Toward the structural genomics of complexes: Crystal structure of a PE/PPE protein complex from *Mycobacterium tuberculosis*. *Proc Natl Acad Sci USA* 103:8060–8065.
45. Ciferri C, et al. (2015) Structural and biochemical studies of HCMV gH/gL/gO and pentamer reveal mutually exclusive cell entry complexes. *Proc Natl Acad Sci USA* 112:1767–1772.
46. Ciferri C, et al. (2015) Antigenic characterization of the HCMV gH/gL/gO and pentamer cell entry complexes reveals binding sites for potently neutralizing human antibodies. *PLoS Pathog* 11:e1005230.
47. McShane MP, Longnecker R (2005) Analysis of fusion using a virus-free cell fusion assay. *Methods Mol Biol* 292:187–196.
48. Omerović J, Lev L, Longnecker R (2005) The amino terminus of Epstein-Barr virus glycoprotein gH is important for fusion with epithelial and B cells. *J Virol* 79:12408–12415.
49. McCoy AJ, et al. (2007) Phaser crystallographic software. *J Appl Crystallogr* 40:658–674.
50. Winn MD, et al. (2011) Overview of the CCP4 suite and current developments. *Acta Crystallogr D Biol Crystallogr* 67:235–242.
51. Bunkóczi G, Read RJ (2011) Improvement of molecular-replacement models with Sculptor. *Acta Crystallogr D Biol Crystallogr* 67:303–312.
52. Adams PD, et al. (2010) PHENIX: A comprehensive Python-based system for macromolecular structure solution. *Acta Crystallogr D Biol Crystallogr* 66:213–221.
53. Lander GC, et al. (2009) Appion: An integrated, database-driven pipeline to facilitate EM image processing. *J Struct Biol* 166:95–102.
54. Mindell JA, Grigorieff N (2003) Accurate determination of local defocus and specimen tilt in electron microscopy. *J Struct Biol* 142:334–347.
55. Ludtke SJ, Baldwin PR, Chiu W (1999) EMAN: Semiautomated software for high-resolution single-particle reconstructions. *J Struct Biol* 128:82–97.
56. Scheres SH (2012) RELION: Implementation of a Bayesian approach to cryo-EM structure determination. *J Struct Biol* 180:519–530.